# Effects of bedplate flexibility on drivetrain dynamics: Case study of a 10 MW spar type floating wind turbine

Shuaishuai Wang [a, *], Amir R. Nejad [a], Erin E. Bachynski [a, b], Torgeir Moan [a, b]

[a] Department of Marine Technology, Norwegian University of Science and Technology (NTNU), Trondheim, NO, 7491, Norway
[b] Centre for Autonomous Marine Operations and Systems (AMOS), Department of Marine Technology, NTNU, Trondheim, NO, 7491, Norway

## ARTICLE INFO

## ABSTRACT

This paper deals with the effect of bedplate flexibility on drivetrain dynamics of a 10 MW spar type floating wind turbine. The 10 MW drivetrain bedplate is designed based on extreme design loads and ultimate limit state (ULS) design criteria. A decoupled analysis approach is employed. Global dynamic analysis of the 10 MW floating turbine is firstly conducted using an aero-hydro-servo-elastic code, then the global response is used as input to the drivetrain dynamic analysis. Load effects and fatigue damage of gears and bearings in the rigid and flexible bedplate models in different environmental conditions are compared. In addition, sensitivity of the drivetrain fatigue damage to varying fidelity in the bedplate modelling is studied. The results indicate that the bedplate flexibility would increase the load effects on bearings inside the gearbox, while it would reduce the load effects on the main bearings. Reasonable bedplate modelling fidelity is of great importance, because it could save a great deal of computational costs without loss of the drivetrain dynamic response accuracy. The present work provides a reference for a proper drivetrain design and dynamic analysis in the future, by accounting for bedplate flexibility.

© 2020 The Authors. Published by Elsevier Ltd. This is an open access article under the CC BY license (http://creativecommons.org/licenses/by/4.0/).

## 1. Introduction

The wind industry, particularly in offshore fields, has been developing quickly in the last decade. The steady and strong wind conditions over deep water locations provide a huge potential of wind energy to be harvested by floating turbines. Since the world's first full scale prototype of floating wind turbine, Hywind [1], was installed in Norway in 2009, there has been increasing attention on floating wind turbines over the past decade. Many studies [2—5] on design and dynamic response analysis of floating wind turbine have been carried out.

The drivetrain, a key part of the wind turbine system, has a high failure rate [6], which directly affects the economic benefits of the wind power. Compared to land-based wind turbine drivetrains, those in floating systems sustain larger loads and more complex load uncertainties caused by the harsh environment. A deep understanding of the loads and load effects of floating wind turbine drivetrains is of vital importance to reduce their fault rate and thus improve their service life as well as reduce their costs. Most studies

on drivetrain are carried out based on land-based wind turbines, while very limited investigations have been conducted on floating wind turbine drivetrains. The dynamics of a 750 KW drivetrain supported on a spar type floating structure were studied by Xing et al. [7,8]. Dynamic responses in floating wind turbines and an equivalent land-based turbine were compared and the results show that the standard deviation of the main shaft loads and gearbox component responses in floating wind turbines are larger than those in land-based turbines. To clarify whether the drivetrains designed for land-based wind turbines can be used in floating turbines, Nejad et al. [9] compared the fatigue damage of a 5 MW drivetrain in land-based and TLP, spar and two semi-submersible floating wind turbines. The results indicate that the main bearings suffer more damage in floating wind turbines than in land-based turbines, and the highest main bearing damage is observed in the spar type floating wind turbine. In another work of Nejad et al. [10], the correlation between the tower-top axial acceleration and drivetrain responses in the spar type floating wind turbine was investigated. A drivetrain dynamic model with flexible planet carrier and ring gear was established by Li et al. [11], and used to study the dynamic characteristics of the drivetrain model under multiple excitation. The results show that the tower shadow has significant influence on the drivetrain dynamics, followed by platform pitch

* Corresponding author.
E-mail addresses: shuaishuai.wang@ntnu.no, shuaiwangcqu@gmail.com (S. Wang).

and surge motions. However, all of these studies modelled the bedplate of the drivetrain as a rigid body.

The bedplate plays a significant role in transmitting non-torque loads from rotor to the tower. For multi-megawatt offshore wind turbines, the bedplate is always subjected to huge non-torque loads primarily produced by the rotor overhang weight and aerodynamic loads, which inevitably lead to some deformation. Because critical components, such as main shaft, gearbox and generator, are directly installed on the bedplate through elastic supports, the deformation of the bedplate would influence drivetrain dynamics. Thus, studying the effects of bedplate flexibility on drivetrain dynamic response gives a better understanding on drivetran dynamic behaviour.

The objective of this study is to study the effects of flexibility of the bedplate on drivetrain load effects and fatigue damage. A detailed 10 MW wind turbine bedplate is designed and a high-fidelity drivetrain dynamic model is established. The present work provides more insight into the dynamic behaviour and hence, enables design optimization of multi-megawatt drivetrains.

## 2. Description of wind turbine and drivetrain concept

### 2.1. Spar type floating wind turbine concept

A 10 MW wind turbine proposed by the Technical University of Denmark (DTU) in 2013 is used in this study. The reference wind turbine (RWT) was designed by upscaling the National Renewable Energy Laboratory (NREL) 5 MW reference turbine [12]. The general specifications of the 10 MW RWT are listed in Table 1. It is noted that the 10 MW RWT proposed by DTU is a land-based concept, and the tower mass presented in Table 1 is for this concept. Since the turbine is considered to be installed on a spar type floating structure in this study, the tower properties are modified to meet fatigue strength, ultimate strength and frequency verifications for the floating system. More detailed information for the 10 MW RWT can be found in the DTU wind energy report written by Bak et al. [13].

The spar platform used in this 10 RWT was designed by Hegseth et al. [5], according to the design for the Offshore Code Comparison Collaboration (OC3) Hywind spar platform, which is defined by Jonkman [14]. The draft of the hull for this 10 MW platform is reduced to 90 m compared to the 120 m in the OC3 Hywind design, which makes it more suitable to be installed in intermediate water depths where the costs of transportation and installation are lower than in deep water. Meanwhile, the hull diameter is increased to provide a sufficient buoyancy. Heavy ballast is placed at the bottom of the hull to stabilize the platform. A mooring system consisting of three catenary lines and clump weights is applied in this model. As in the OC3 model, a rotational spring is added to achieve a sufficient

yaw stiffness of the mooring system. The fairleads are placed at the same depth as the center of gravity (COG) of the entire wind turbine system. The main properties of the platform and mooring system are presented in Table 2 and Table 3, respectively, and illustrated in Fig. 1. More detailed information for the spar platform can be found in the study of Hegseth and Bachynski [5].

### 2.2. Drivetrain concept

A 10 MW medium-speed wind turbine drivetrain, which is designed by Wang et al. [15,16] with a rigid bedplate, is used in this study. The 10 MW drivetrain mainly consists of a hub, a main shaft, a gearbox, an elastic generator coupling, a bedplate and a generator. Firstly, the rotor blades convert wind energy into mechanical energy, which is then transmitted through the hub and the main shaft to the gearbox. Further, the gearbox transforms the low-speed and high-torque mechanical energy to high-speed and low-torque form. Finally, the mechanical energy output from the gearbox is driven by the elastic coupling to the generator to generate electricity. The drivetrain schematic layout and topology with gear and bearing nomenclature are shown in Figs. 2 and 3, respectively.

The drivetrain is designed as a four-point support layout, namely two main bearings and two torque arm supports. Ideally, all the non-torque loads from the rotor side could be carried by the two main bearings and transmitted to the tower through the bedplate, thus this layout could effectively reduce non-torque loads entering into the gearbox. The gearbox is designed as a conventional configuration that consists of two planetary stages and one parallel stage. In the two planetary stages, ring gears are fixed on the gearbox housing, which is supported on the bedplate via torque arms. Input torque is applied to the planet carriers and sun gears serve as the output torque. In the third parallel stage, torque is delivered from the sun gear of the second planetary stage to generator coupling through the high-speed gear pair (Gear-Pinion in Fig. 3). Critical drivetrain components - gears and bearings - are designed based on design loads and criteria defined in relevant international design standards. Table 4 presents the drivetrain specifications. More details for the drivetrain design procedure and parameters are presented in the previous works [15,16].

## 3. Analysis methodology

This section presents the analysis approach for drivetrain dynamics. Fig. 4 shows the flow chart of the analysis methodology of the study. Firstly, the 10 MW wind turbine bedplate is designed based on the design basis, loads and criteria defined by relevant international standards. Further, a finite element model of the bedplate is integrated with other drivetrain components, to form a high-fidelity drivetrain dynamic model. Then, the decoupled

**Table 1**
Specifications of the DTU 10 MW reference wind turbine [13].

| Parameter | Value |
|---|---|
| Type | Upwind/3 blades |
| Control | Collective pitch |
| Rated power (MW) | 10 |
| Cut in, rated and cut out wind speed (m/s) | 4, 11.4, 25 |
| Rotor diameter (m) | 178.3 |
| Hub height (m) | 119.0 |
| Hub diameter (m) | 5.6 |
| Hub overhang (m) | 7.1 |
| Shaft tilt angle (deg) | 5.0 |
| Rotor mass (kg) | 227,962 |
| Nacelle mass (kg) | 446,036 |
| Tower mass[a] (kg) | 628,442 |

[a] Mass for land-based tower in DTU wind energy report.

**Table 2**
Main properties of the spar buoy [5].

| Parameter | Value |
|---|---|
| Water depth (m) | 320 |
| Draft (m) | 90 |
| Elevation of platform top above SWL (m) | 10 |
| Depth to top of taper below SWL (m) | 4 |
| Depth to bottom of taper below SWL (m) | 12 |
| Platform diameter above taper (m) | 8.3 |
| Platform diameter below taper (m) | 15 |
| Hull mass, including ballast (kg) | $1.33 \times 10^7$ |
| CoG location below SWL (m) | −56.3 |
| CoB location below SWL (m) | −47.8 |

SWL: still water level; CoG: Center of gravity of entire wind turbine system; CoB: Center of buoyancy.

**Table 3**
Main properties of the mooring system [5].

| Parameter | Value |
| --- | --- |
| Unstretched mooring line length (m) | 902.2 |
| Fairlead location below SWL (m) | −56.3 |
| Radius to anchors (m) | 855.2 |
| Equivalent mooring line axial stiffness (kN) | $3.84 \times 10^5$ |
| Additional yaw spring stiffness (kN/rad) | $1.48 \times 10^5$ |

dynamic response analysis is conducted. The global dynamic response analysis of the spar type floating wind turbine is firstly carried out under different wind and wave conditions, then forces and moments at the tower top as well as generator speed are extracted. The loads at the tower top are then converted to the hub center position in the drivetrain model. Meanwhile, the generator torque is controlled on the generator rotor shaft via a proportional-integral (PI) controller based on the generator speed, to conduct the drivetrain dynamic analysis. Next, time series of drivetrain gear and bearing load effects are obtained, and finally the gear and bearing response statistics are calculated and fatigue damage is estimated based on methods in gear and bearing international standards. More detailed introduction to the bedplate design, floating wind

turbine and drivetrain dynamic models, decoupled dynamic analysis method and gear and bearing fatigue damage estimation methods is given in the following sections.

### 3.1. Bedplate design

The bedplate is designed based on ultimate limit state (ULS) criteria using a simplified structural design approach. Detailed material parameters, design load cases description and extreme design loads for the bedplate design are listed in Tables A1, A2 and A3 in the appendix, respectively. An initial size of the bedplate is firstly determined based on the dimension of the detailed drivetrain model that was used in the study of Wang et al. [16]. Then, an iterative optimization process is conducted based on the ULS design criteria. According to the international standard IEC 61400−4 [17], the safety of the bedplate is defined by the load reverse factor for ultimate strength, $LRF_u$, which is calculated by the following Equation:

$$LRF_u = \frac{\sigma_{lim}}{\sigma_{max} \cdot \gamma_n} \geq 1 \qquad (1)$$

where $\sigma_{max}$ is the maximum linear elastic stress represented by von
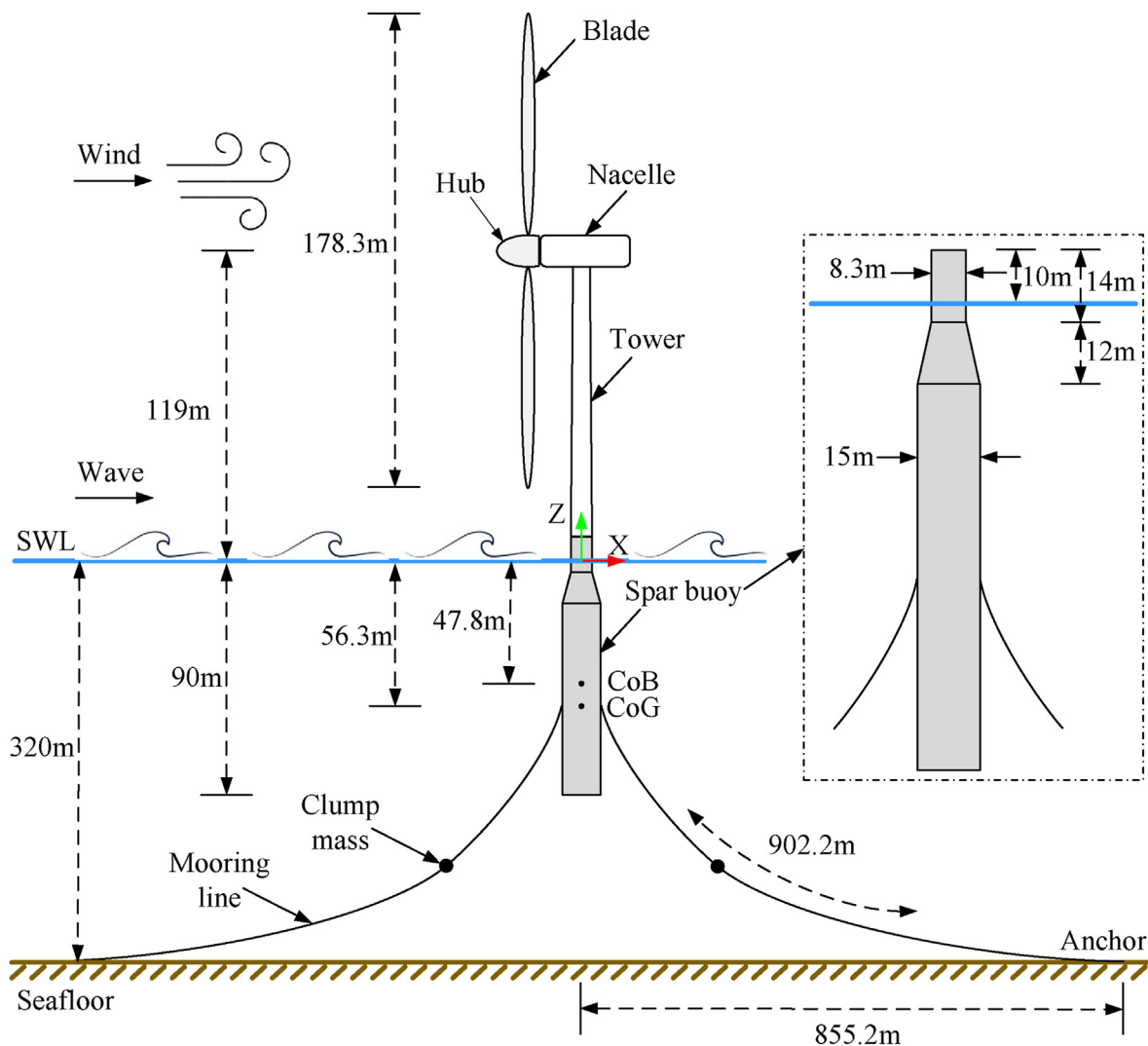


**Fig. 1.** 10 MW spar type floating wind turbine.
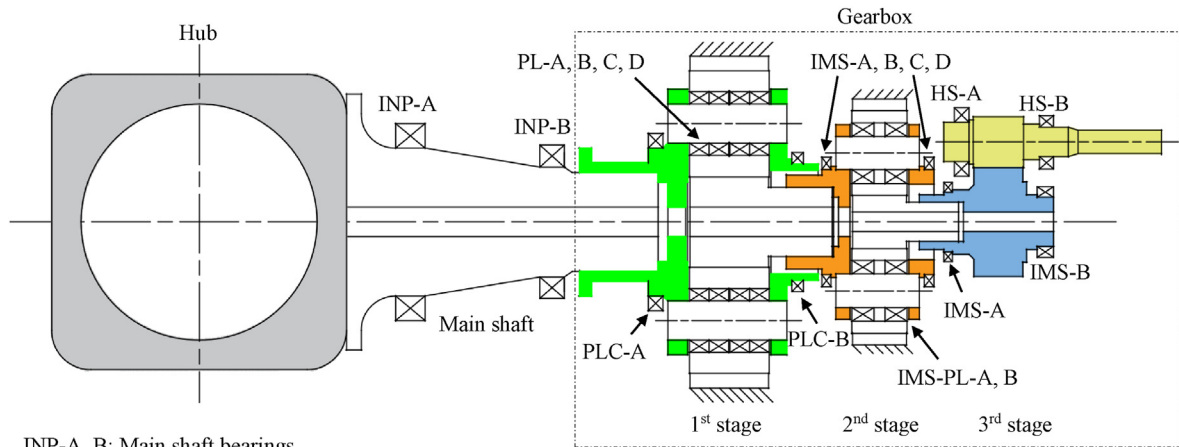
INP-A, B: Main shaft bearings.
PLC-A, B: Planet carrier bearing in the first stage; PL-A, B, C, D: Planet bearings in the first stage.
IMS-PLC-A, B: Planet carrier bearing in the second stage; IMS-PL-A, B: Planet bearings in the second stage.
IMS-A, B: Intermediate shaft bearings in the third stage; HS-A, B: High speed shaft bearings in the third stage.

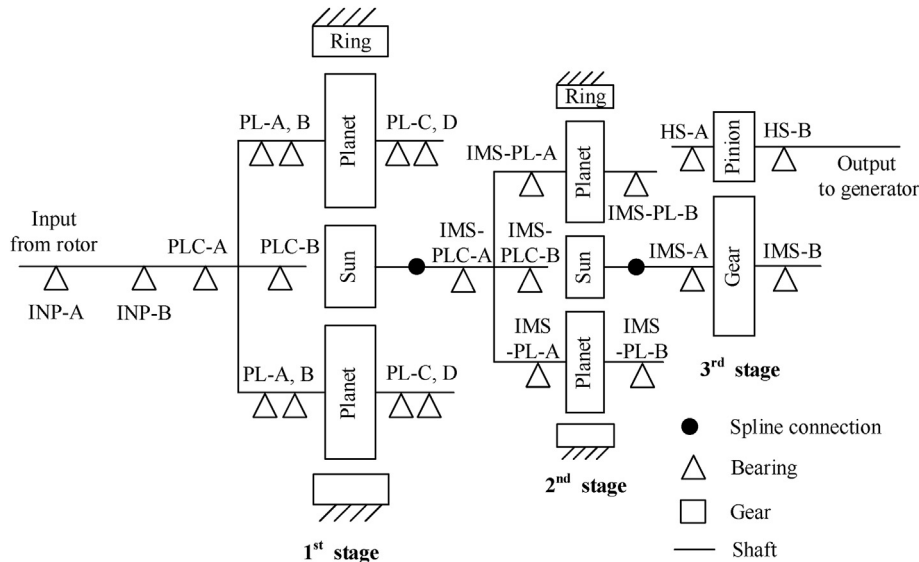Fig. 2. 10 MW reference wind turbine drivetrain schematic layout.



Fig. 3. 10 MW reference drivetrain topology.

**Table 4**
10 MW reference wind turbine drivetrain specifications [16].

| Parameter | Value |
| --- | --- |
| Drivetrain type | Four-point support |
| Gearbox type | Two planetary + one parallel |
| First stage ratio | 4.423 |
| Second stage ratio | 5.192 |
| Third stage ratio | 2.179 |
| Total ratio | 50.039 |
| Designed power (MW) | 10 |
| Rated input shaft speed (rpm) | 9.6 |
| Rated generator shaft speed (rpm) | 480.4 |
| Rated input shaft torque (KN.m) | 9947.9 |
| Rated generator shaft torque (KN.m) | 198.8 |
| Drivetrain dry mass (× 1000 kg) | 141.54 |
| Gearbox dry mass (× 1000 kg) | 60.43 |
| Maximum gear outer diameter (m) | 3.098 |
| Gearbox length (m) | 5.964 |
| Designed service life (year) | 20 |

Mises stress, which is calculated by the finite element analysis in ANSYS in this study. $\sigma_{lim}$ is the maximum local stress that the component can withstand; according to the bedplate yield strength in Table A1 and the partial safety factor for material that is defined in IEC 61400−1 [18], the $\sigma_{lim}$ is taken as 200 MPa $\gamma_n$ is the partial factor for the consequence of the failure; according to the IEC 61400−1 [18], the $\gamma_n$ of bedplate shall be consistent with component class 2, which is equal to 1.

Fig. 5 shows the 10 MW bedplate finite element model and loads. In order to accurately assess the bedplate ultimate strength, a section of tower is also established, which links to the bedplate via a constraint. Additionally, the acting loads, which are extracted from a complete drivetrain model via static balance analysis in SIMPACK [19], are applied at the interface nodes of the bedplate which are connected with main bearings, torque arms and generator supports. Fig. 6 illustrates the von Mises stress distributions of the bedplate under design load case DLC1, which is considered as an example case in this study. It is seen that the maximum von
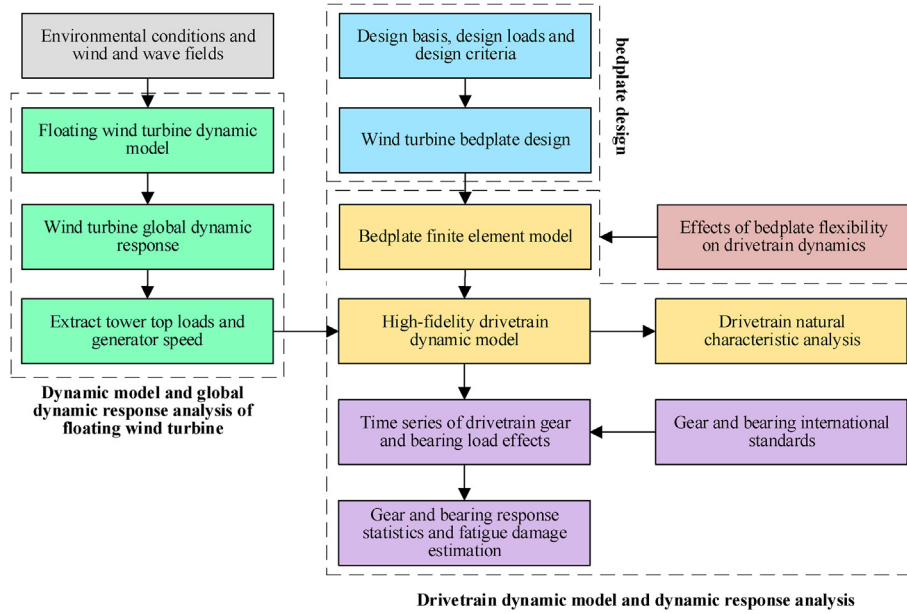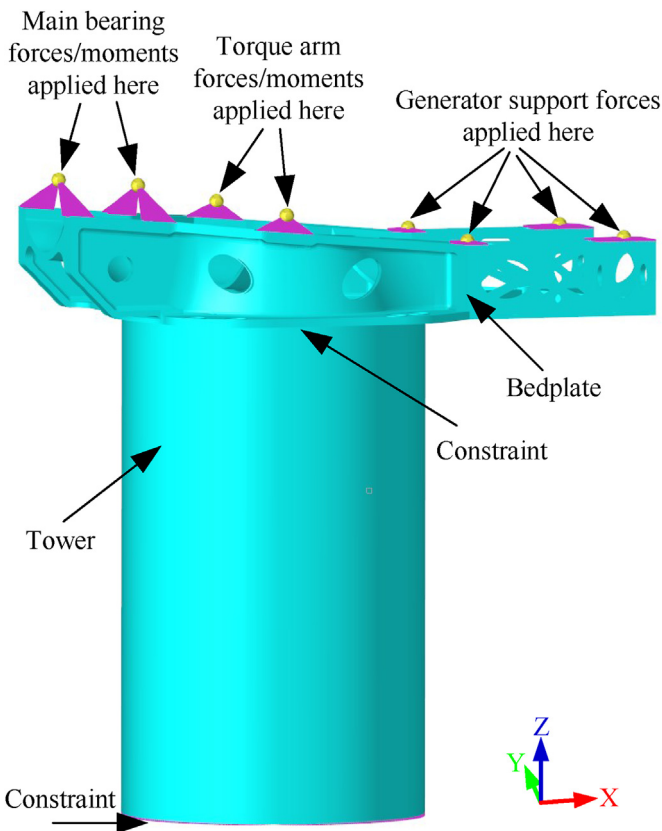
Fig. 4. Flow chart of the analysis methodology.



Fig. 5. 10 MW bedplate finite element model and load application.



Fig. 6. Von Mises stress distribution of the bedplate under design load case DLC1.

**Table 5**
Bedplate maximum von Mises stresses and corresponding $LRF_u$s under all design load cases.

| Design load case | DLC1 | DLC2 | DLC3 | DLC4 | DLC5 | DLC6 |
|---|---|---|---|---|---|---|
| M.vMs (MPa) | 156.65 | 193.32 | 150.02 | 141.60 | 189.28 | 198.08 |
| $LRF_u$ | 1.28 | 1.03 | 1.33 | 1.41 | 1.06 | 1.01 |
| **Design load case** | **DLC7** | **DLC8** | **DLC9** | **DLC10** | **DLC11** | **DLC12** |
| M.vMs (MPa) | 179.46 | 183.44 | 195.56 | 167.92 | 159.34 | 165.93 |
| $LRF_u$ | 1.11 | 1.09 | 1.02 | 1.19 | 1.26 | 1.21 |

M.vMs: Max. von Mises stress.

Mises stress of the bedplate is less than the yield strength under the DLC1 and the main stress is located in the front area where the main shaft is installed. The von Mises stress distributions of the bedplate under all design load cases are demonstrated in Fig. 17 in appendix. Table 5 lists the maximum von Mises stresses of the bedplate and their corresponding $LRF_u$s under all design load cases.
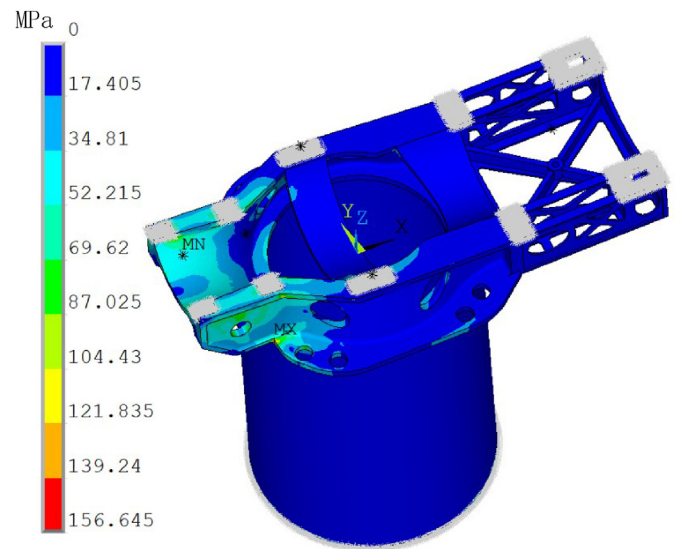
The $LRF_u$s are larger than 1 under all load cases, which satisfies the design requirement defined in IEC 61400−4 [17]. After carrying out the iterative optimization design, the final mass of the 10 MW

bedplate is 102.39 tons.

## 3.2. Numerical model of the wind turbine system

### 3.2.1. Spar floating wind turbine model

The numerical model of the 10 MW spar type floating wind turbine is established using SIMO-RIFELX, a time domain fully coupled aero-hydro-servo-elastic simulation tool, developed by SINTEF Ocean. SIMO [20] calculates the rigid body hydrodynamic loads on the floating structures. RIFLEX [21] serves as a nonlinear finite element solver to calculate the dynamic response of the flexible elements as well as the aerodynamic loads based on the Blade Element/Momentum (BEM) theory, including Prandtl and Glauert corrections, dynamic stall, tower shadow, and skewed wake corrections, and provide the link to an external controller. The external controller, which is written in Java, is used to control generator torque and blade pitch. The SIMO-RIFLEX wind turbine module has been verified by Ormberg et al. [22] and Luxcey et al. [23], and applied in OC5 project [24].

The hull, hub and nacelle are modelled with rigid bodies in the floating wind turbine model. The blades, tower and shafts are considered as nonlinear elastic beam elements, while the mooring lines are represented by nonlinear bar elements with only axial stiffness. The drivetrain in the global wind turbine model is modelled as a single degree-of-freedom (DOF) torsional spring-damper system. The rotor and generator are connected to each other via a torsional spring-damper joint. The torsional moments of inertia of the rotor and the generator are considered, where the generator moment of inertia is an effective value that is calculated by scaling original value with the square of the drivetrain gear ratio. The stiffness and damping of the spring-damper system are determined by means of the drivetrain first-order torsional natural frequency. The two bodies are linked to the reference frame with only one rotational DOF. A detailed description of the simplified drivetrain model is given in the work of Oyague [25]. The numerical floating wind turbine model and the coordinate system are illustrated in Fig. 7.

### 3.2.2. Drivetrain dynamic model and natural modes

The drivetrain dynamic model is established via the multi-body system (MBS) approach in this study. The drivetrain components are represented by various rigid and flexible bodies in the MBS, and these bodies are linked by means of joints and kinematic constraints, which allow or restrict their motions. The forces and moments in the MBS are provided by specific excitation elements. The dynamic behaviour of the MBS is obtained by solving the motion of the system due to the applied forces and the inertia characteristics of the bodies. Detailed descriptions about the MBS modelling approach are provided by Oyague [25] and Wang et al. [16]. A MBS simulation software, SIMPACK [19], is used for the drivetrain numerical modelling and dynamic analysis. SIMPACK is a state-of-the-art simulation analysis software to describe and predict the dynamic behaviour of mechanical and mechatronic system; it enables simulation of non-linear motion of the system. The basic principle is to build a dynamic model of a mechanical or mechatronic system, where bodies are linked by joints, constraints and force elements, then he SIMPACK solver is used to obtain the dynamic response of the system under external excitation. This dynamic simulation tool has been widely used for wind turbine drivetrain analysis and verified against various publicly available studies (e.g. Ref. [26–29]).

In order to accurately describe the dynamic behaviour of the drivetrain model, the critical components, bedplate, tower, planet carriers and shafts, are treated as reduced finite element (FE) bodies. These FE models are established in ANSYS. A modal reduction technique, Craig Bampton component mode synthesis (CMS) method [30], is employed to reduce the huge number of DOFs in those FE models. Moreover, a flexible multi-point constraint (MPC) method, which has been used in many studies (e.g. Refs. [31–34]), is adopted to achieve the coupling between the condensed FE model and other components in the drivetrain MBS model. Gears are established with gear geometry parameters, such as number of gear teeth, gear normal module, normal pressure angle, helix angle, gear flank widthï¼Œ addendum and dedendum coefficients, which are obtained from the drivetrain design and detailed parameters are provided in the previous work [16]. Gear tooth contact is modelled by a specific force element, FE225, in SIMPACK which accounts for the stiffness force, the damping force and the friction force. Bearing forces and moments are calculated via a 6-DOF force element, FE 43, in SIMPACK, where a linear force-displacement relation based on bearing stiffness value is considered in this study. The bearing stiffness is represented as a 6-DOF linear diagonal stiffness matrix, which is shown as below:

$$\mathbf{K} = \begin{pmatrix} K_{xx} & 0 & 0 & 0 & 0 & 0 \\ & K_{yy} & 0 & 0 & 0 & 0 \\ & & K_{zz} & 0 & 0 & 0 \\ & & & K_{\alpha\alpha} & 0 & 0 \\ & sym. & & & K_{\beta\beta} & 0 \\ & & & & & K_{\gamma\gamma} \end{pmatrix} \quad (2)$$

where $K_{xx}$, $K_{yy}$ and $K_{zz}$ represent the axial, tangential and radial stiffness respectively, with units in N/m. The $K_{\beta\beta}$ and $K_{\gamma\gamma}$ represent pitch and yaw stiffness respectively, with unit in Nm/rad. The $K_{\alpha\alpha}$ is 0, because α corresponds to bearing rotational direction. The off-diagonal terms are zeros, because cross-coupling of forces and moments between the directions is not considered in this work. Bearing stiffness values are provided in the previous study [16].

The 10 MW drivetrain dynamic model is presented in Fig. 8. An 18-m-long flexible tower is established in this model, instead of the entire tower of the 10 MW floating turbine, to couple with the flexible bedplate and serve as the boundary conditions of the drivetrain model. Fig. 9 compares the eigenmodes of the drivetrain system for the rigid and the flexible bedplate models. The detailed eigenfrequencies and mode description are presented in Table 6. The study focuses on the coupled rotor-drivetrain-bedplate-tower modes that are within low frequency range, since drivetrain resonances are most likely to occur in these modes under the low frequency load excitation from the rotor. In the rigid bedplate model, the drivetrain system modes are of three types: torsion, horizontal and vertical bending, and these modes coupled with tower bending. As a contrast, with the modelling of the flexible bedplate, the coupled drivetrain system modes are bedplate vertical bending, bedplate torsion, drivetrain and bedplate torsion, drivetrain horizontal bending and bedplate torsion as welll as drivetrain and bedplate vertical bending, and these modes coupled with tower bending. Another observation is that with the modelling of the flexible bedplate, eigenfrequencies of the drivetrain system generally decrease from the rigid model, especially for those of bending modes, they decrease from 4.31 Hz to 5.14 Hz to 4.01 and 4.54 Hz, respectively.

## 3.3. Dynamic response analysis of the wind turbine system

A two-step decoupled analysis approach, as illustrated in Fig. 10, is carried out to determine the drivetrain dynamic response. First, the global aero-hydro-servo-elastic analysis of the floating wind turbine with the simplified single DOF drivetrain is carried out in SIMO-RIFLEX. The time series of loads experienced by drivetrain in the global simulation are then used as input to the multi-body
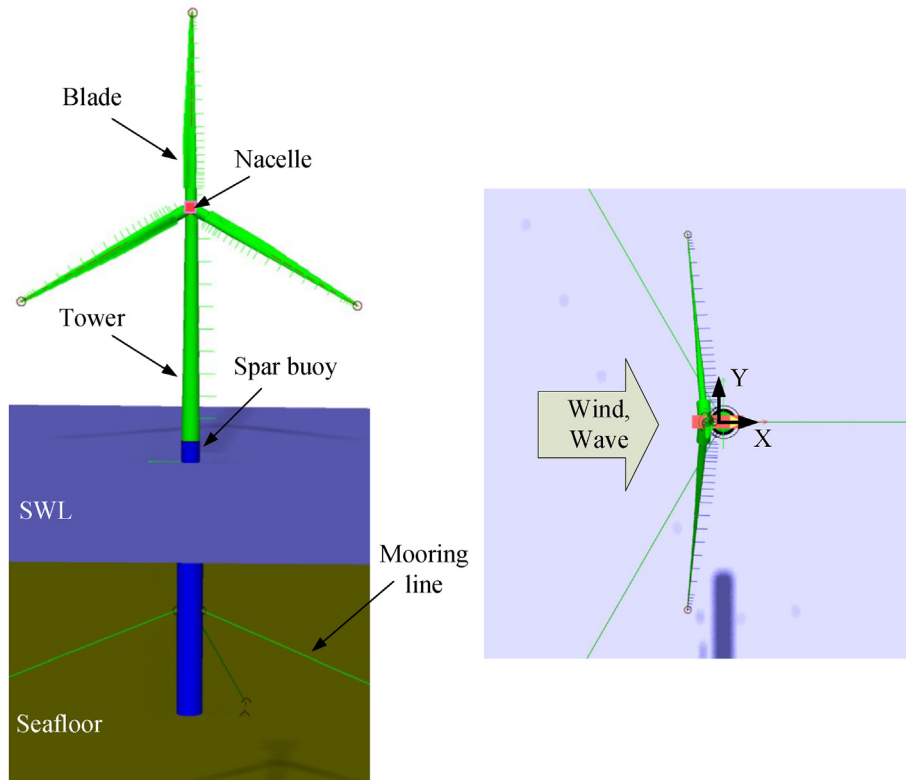
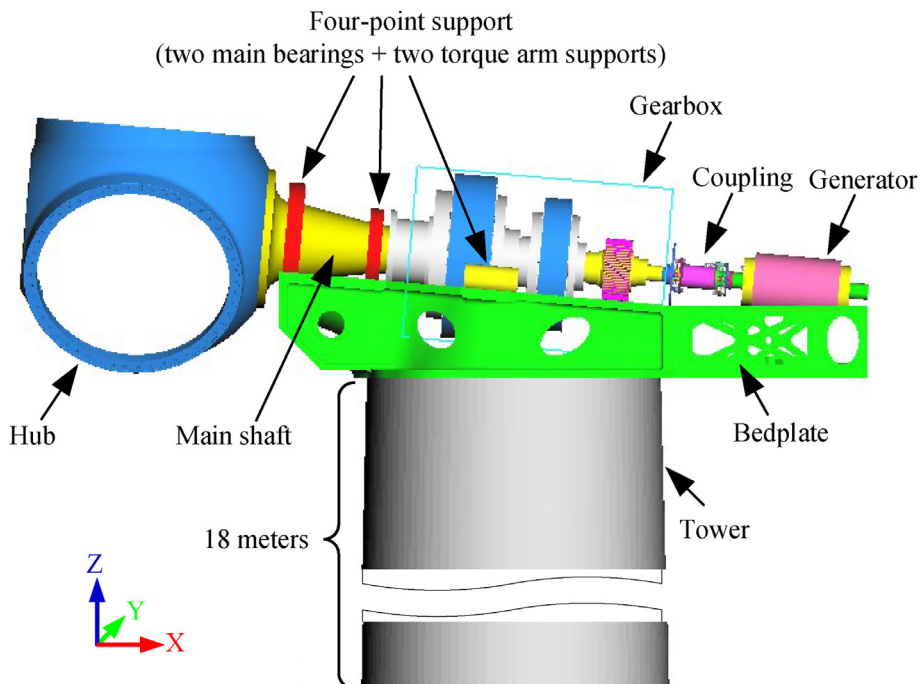**Fig. 7.** 10 MW spar type floating wind turbine numerical model.



**Fig. 8.** 10 MW drivetrain numerical model.

drivetrain model in SIMPACK to conduct the drivetrain dynamic response analysis. The decoupled approach has been effectively used in earlier studies [35–37]. A detailed introduction of the global analysis and the drivetrain load effect analysis is given in the following sections.

### 3.3.1. Global analysis

The time domain global aero-hydro-servo-elastic dynamic response analysis of the floating wind turbine is conducted in SIMO-RIFLEX, which accounts for the wind turbine aerodynamics, hydrodynamics, structural dynamics and controller dynamics.
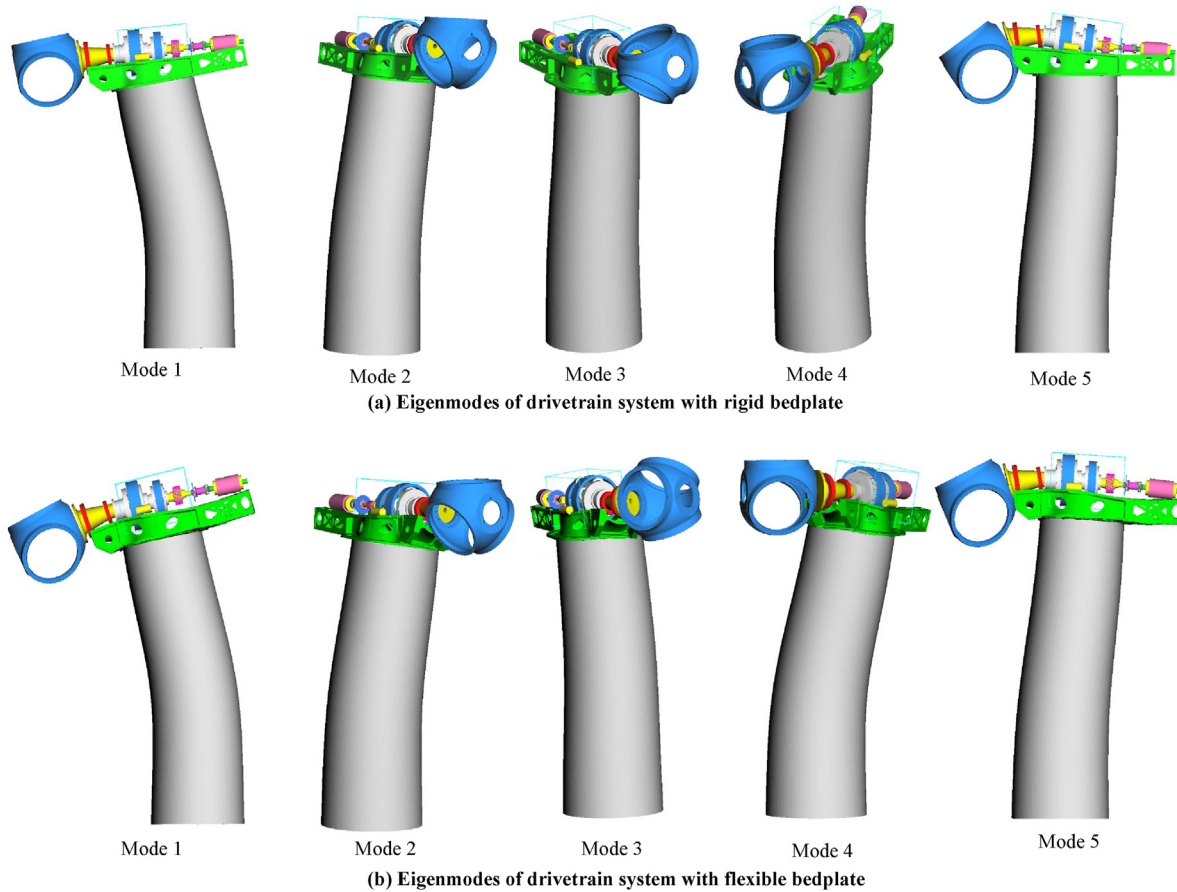
(a) Eigenmodes of drivetrain system with rigid bedplate



(b) Eigenmodes of drivetrain system with flexible bedplate

Fig. 9. 10 MW drivetrain system eigenmodes.

**Table 6**
Eigenmodes of the 10 MW drivetrain model with rigid or flexible bedplate.

| Mode | Bedplate | E_freq. (Hz) | Mode description |
|---|---|---|---|
| | rigid | 2.98 | Tower fore-aft bending |
| 1 | flexible | 2.72 | Tower fore-aft bending and bedplate vertical bending |
| | rigid | 2.98 | Tower side-side bending |
| 2 | flexible | 2.86 | Tower side-side bending and bedplate torsion |
| | rigid | 3.67 | Tower side-side bending and drivetrain torsion |
| 3 | flexible | 3.54 | Tower side-side bending and drivetrain and bedplate torsion |
| | rigid | 4.31 | Tower side-side bending and drivetrain horizontal bending |
| 4 | flexible | 4.01 | Tower side-side bending, drivetrain horizontal bending and bedplate torsion |
| | rigid | 5.14 | Tower fore-aft bending and drivetrain vertical bending |
| 5 | flexible | 4.54 | Tower fore-aft bending and drivetrain and bedplate vertical bending |

Hydrodynamic loads on the hull are considered by a combination of potential flow theory and Morison's equation. According to the potential flow theory, the frequency-dependent added mass, radiation damping, and first-order wave forces are obtained in the frequency domain using a panel model, and are then applied in the time domain using convolution. Viscous forces are calculated through the drag term in the Morison's equation. In addition, the hydrodynamic loads on the mooring lines are modelled by Morison's equation. Second order wave forces are not included in the present study.

Aerodynamic loads acting on the blades are calculated using BEM theory, which combines the balde element theory and momentum theory and is the most commonly used method for calculating aerodynamic forces on rotor blades. Glauert, Prandtl tip loss, Øye dynamic inflow and Øye dynamic stall corrections are taken into account to incorporate the aerodynamic effects of large induced velocity, tip losses, dynamic inflow and dynamic stall. Aerodynamic loads on the tower or nacelle are not included in the present work.

The wind turbine controller applied in this study is based on the original controller for the 10 MW wind turbine that is defined by DTU, where both blade pitch angle control and generator control are included. In order to avoid large transient response caused by negative damping effects on platform motions, proportional and integral gains are modified for this spar type floating turbine, as described in the study of Hegseth and Bachynski [5].

### 3.3.2. Drivetrain load effect analysis

As shown in Fig. 10, the forces and moments at the tower top obtained from the global analysis are converted and applied at the
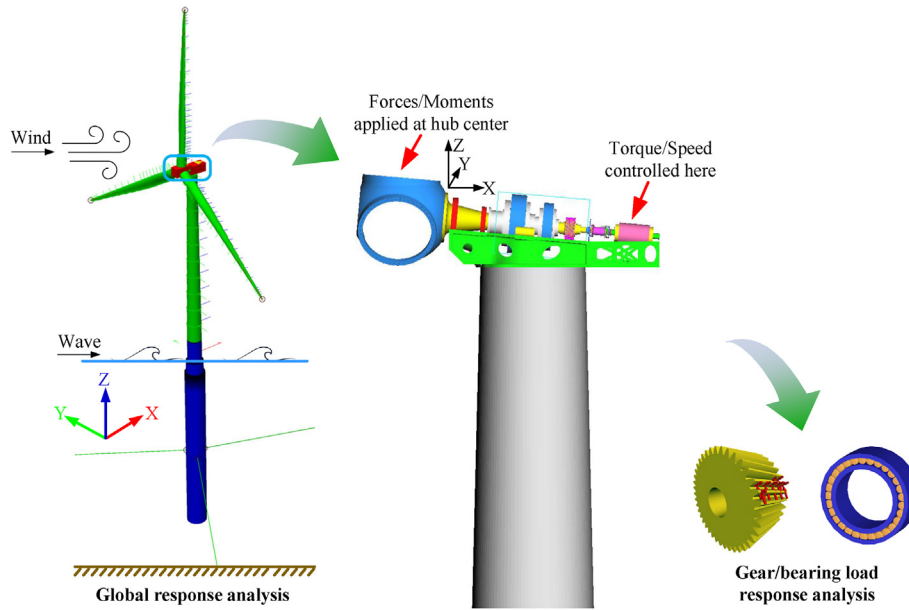
**Fig. 10.** Decoupled approach for wind turbine drivetrain analysis.

hub center of the drivetrain MBS model. Moreover, the generator feedback torque is applied on the generator rotor shaft, which is calculated by a PI velocity controller, as described by Xing et al. [8]. Then, the drivetrain dynamic simulation is carried out, and load effects of gears and bearings are further investigated.

### 3.4. Fatigue damage estimation for bearings and gears

Bearings and gears are the most vulnerable components in a wind turbine drivetrain, because they are affected by stochastic turbulent wind and irregular waves as well as time-varying gear meshing stiffness and transmission errors. Fatigue damage estimation for bearings and gears is a good measure of drivetrain dynamic performance. In this study, 1-h short-term fatigue damage of drivetrain gears and bearings is estimated in different environmental conditions and they are represented by damage equivalent fatigue load (DEFL). DEFL is a constant-amplitude load, which can produce equivalent fatigue damage to that of the load spectrum. DEFL calculation is a good measure to estimate short-term fatigue damage of bearings and gears and to understand the relationship between response statistics of bearings and gears and their fatigue damage.

#### 3.4.1. Bearing fatigue damage estimation

Fig. 11 illustrates a three-step process of DEFL calculation of bearings from time series of bearing loads and load duration distribution. First, the time series of bearing dynamic equivalent load $P$, which is related to bearing lifetime based on extensive experiments, is calculated by the formula from the international standard ISO 281 [38]:

$$P = XF_r + YF_a \tag{3}$$

where $F_r$ and $F_a$ are time series of radial and axial loads of the bearing, respectively, which are obtained from the drivetrain dynamic simulations. $X$ and $Y$ are dynamic loading factors, which depend on bearing designation and are obtained from the bearing standard ISO 281 [38].

Then, the time series of bearing dynamic equivalent loads are divided into load bins, which are composed of many constant loads

and the total duration of each constant load, as shown from Fig. 11 (a)–(b). The upper level of the load range in the load time series is used as the constant load in load bin. The load bin of $P_2$ associated with $t_1 + t_2$ is taken as an example. The upper level load $P_2$ is used as the constant load value in the load bin of $P_2$ associated with $t_1 + t_2$ when the loads in time periods $t_1$ and $t_2$ are located between $P_2$ and $P_3$. Hereby the bearing load duration distribution (LDD) is created. The LDD method will lead to a conservative results, while the extent of conservatism depends on the number of load bins. Next, the load bins associated with time are related to cycles, as shown from Fig. 11 (b)–(c), based on the formula:

$$l_i = \sum_j \frac{t_j w_{bj}}{2\pi} \tag{4}$$

where $l_i$ is the number of load cycles in the load bin $i$. $t_j$ is the $j$-th time duration of the load bin $i$. $w_{bj}$ is average bearing rotational speed (rad/s) in $j$-th time duration of the load bin $i$. The time series of bearing rotational speed is obtained from the drivetrain dynamic simulations.

Finally, the bearing DEFL is calculated by the formula obtained from Ref. [39]:

$$DEFL = \left[ \frac{\sum_i p_i^a l_i}{\sum_i l_i} \right]^{1/a} \tag{5}$$

where $a$ is the bearing life factor, $a = 3$ for ball bearings and $a = \frac{10}{3}$ for roller bearings.

#### 3.4.2. Gear fatigue damage estimation

Based on the international standard, IEC61400-4 [17], of design requirements for wind turbine gearboxes, gear design mainly depends on surface pitting resistance and tooth root bending strength, which shall be estimated based on gear international codes ISO 6336−2 [40] and ISO 6336−3 [41], respectively. According to authors' previous study [16], gear tooth bending fatigue damage is much more severe than pitting fatigue damage in the 10 MW drivetrain model. Therefore, the gear tooth bending fatigue damage is estimated in this study. The damage equivalent fatigue
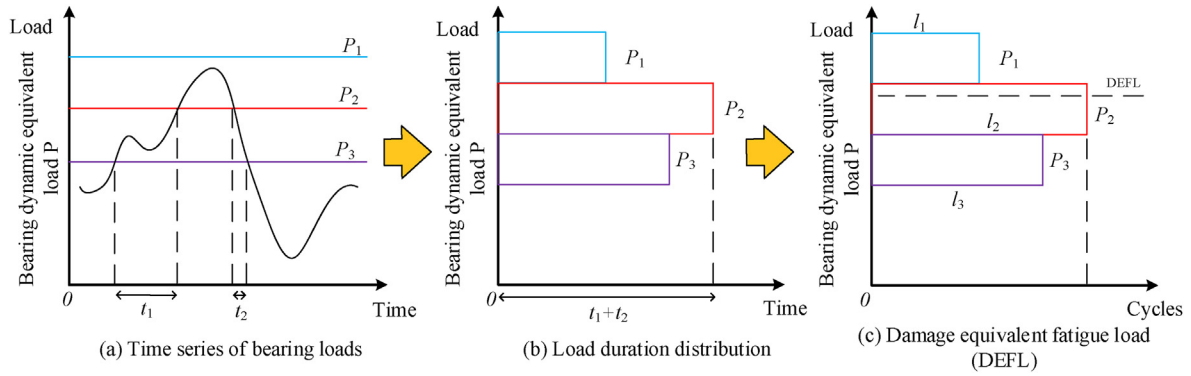
Fig. 11. Damage equivalent fatigue load calculation of bearings from load time series and load bins.

bending stress (DEFS) for gears is addressed via a similar procedure as the bearing DEFL calculation. Firstly, time series of gear tooth root bending stresses are calculated based on gear mesh forces extracted from drivetrain dynamic simulations, according to the method in the gear standard ISO 6336–3 [41]. Then, the time series of gear tooth root bending stresses are divided into stress bins based on the procedure shown in Fig. 11. Next, in each stress bin, the number of gear tooth bending stress cycles is calculated via the following formula:

$$n_i = \sum_j \frac{t_j w_{gj}}{2\pi} \qquad (6)$$

where $n_i$ is the number of stress cycles in the stress bin $i$. $t_j$ is the $j$-th time duration of the bin $i$, and $w_{gj}$ is the average gear rotational speed (rad/s) in the $j$-th time duration of the bin $i$. Because the gearbox has five planets in the first stage and three planets in the second stage, for each rotation, the sun gear and the ring gear will encounter five contacts with planets in the first stage and three in the second stage, thus five times and three times stress cycles are considered for the sun gears and ring gears in the first and the second stages, respectively.

Similar to bearing DEFL calculation, the gear DEFS is calculated by the formula obtained from Ref. [39]:

$$DEFS = \left[ \frac{\sum_i s_i^m n_i}{\sum_i n_i} \right]^{1/m} \qquad (7)$$

where $s_i$ is gear tooth root bending stress in the stress bin $i$. $m$ is a gear S–N curve parameter that is related to gears' material and heat treatment and is calculated based on gear standards ISO 6336–3 [41] and ISO 6336–5 [42].

### 3.5. Environmental conditions and load cases

A representative location in the Northern North Sea, site 14 in the study of Li et al. [43], is assumed to be the floating wind turbine site. All the environmental conditions are selected based on a long-term joint distribution for 10 years' hindcast wind and wave data.

Five load cases, which are in normal operational conditions, are selected for simulations in this study, as listed in Table 7. The wind speeds are selected to cover a range of operational conditions, while the corresponding sea state consists of the most probable significant wave height ($H_s$) and wave peak period ($T_p$) for the given hub height wind speed ($u$). The probability distribution of the wind speed at hub height is illustrated in Fig. 12, where the selected five load cases are marked. For each load case, five independent

**Table 7**
Load cases in the normal operational conditions.

| Load case | LC1 | LC2 | LC3 | LC4 | LC5 |
|---|---|---|---|---|---|
| u (m/s) | 5 | 8 | 12 | 16 | 24 |
| $H_s$ (m) | 1.6 | 1.9 | 2.5 | 3.3 | 5.4 |
| $T_p$ (s) | 9.4 | 9.7 | 10.1 | 10.7 | 11.9 |

simulations with random seeds are conducted. Each simulation is carried out for 4000s, and the first 400s are removed to avoid start-up transient effects.

The wind files are generated using the TurbSim program [44] according to the Kaimal turbulence model applying for Class B turbines defined in the IEC 61400–1 [18]. The mean wind speed $u$ at the hub height of reference 10 MW turbine is calculated using a power law profile with exponent 0.14, as recommended in IEC 61400–3 [45]. Wave time series are generated using the JONSWAP (Joint North Sea Wave Project) spectrum, which is described in IEC 61400–3 [45], with given $H_s$ and $T_p$. It is assumed that wind and waves are aligned in the positive wind direction, and current is not considered in this study.

## 4. Results and discussions

### 4.1. Global dynamic response

Time varying forces and moments at the tower top are obtained from the global simulation, then they are converted to the hub center position to conduct the drivetrain dynamic response analysis. Fig. 13 shows the mean values and standard deviations of forces and moments at the hub center under the five load cases. The coordinates used in this figure are shown in Fig. 10. The mean torque $M_x$ should be constant even if the wind speed is still increasing after the rated condition, but it is seen to decrease slightly. The most probable reason for this is that the control system is not calibrated perfectly to this floating wind turbine model. The largest mean value of thrust force $F_x$ occurs at the rated condition, while the absolute mean values of bending moments $M_y$ and $M_z$ increase with the load case increases.

Large standard deviations are observed in the lateral force $F_y$ and the vertical force $F_z$ as well as the bending moments $M_y$ and $M_z$, and in general, they increase with the load case increases. FFT analysis of those forces and moments under load cases LC3 is conducted to reveal the reason of the load variation, which is illustrated in Fig. 14. The low-frequency wind-induced turbulent response and the wind turbine pitch resonant response dominate
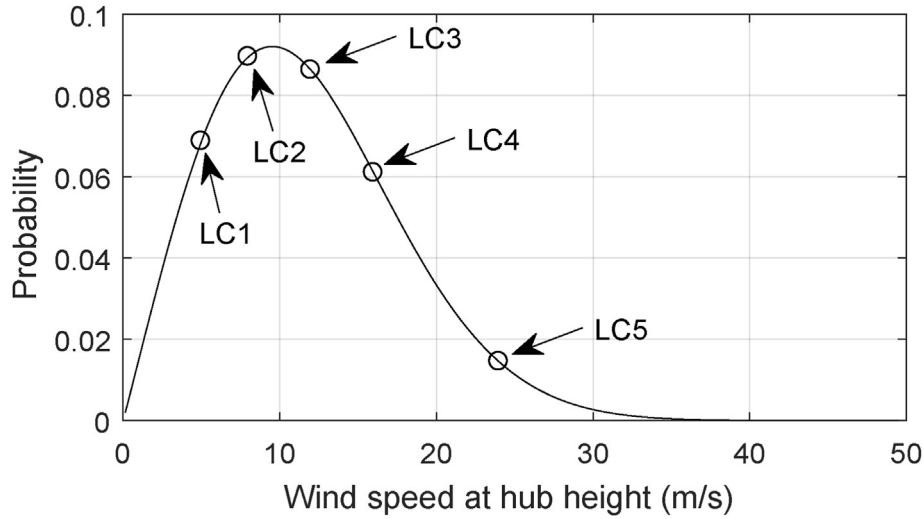
**Fig. 12.** Probability distribution of wind speed at wind turbine hub height.
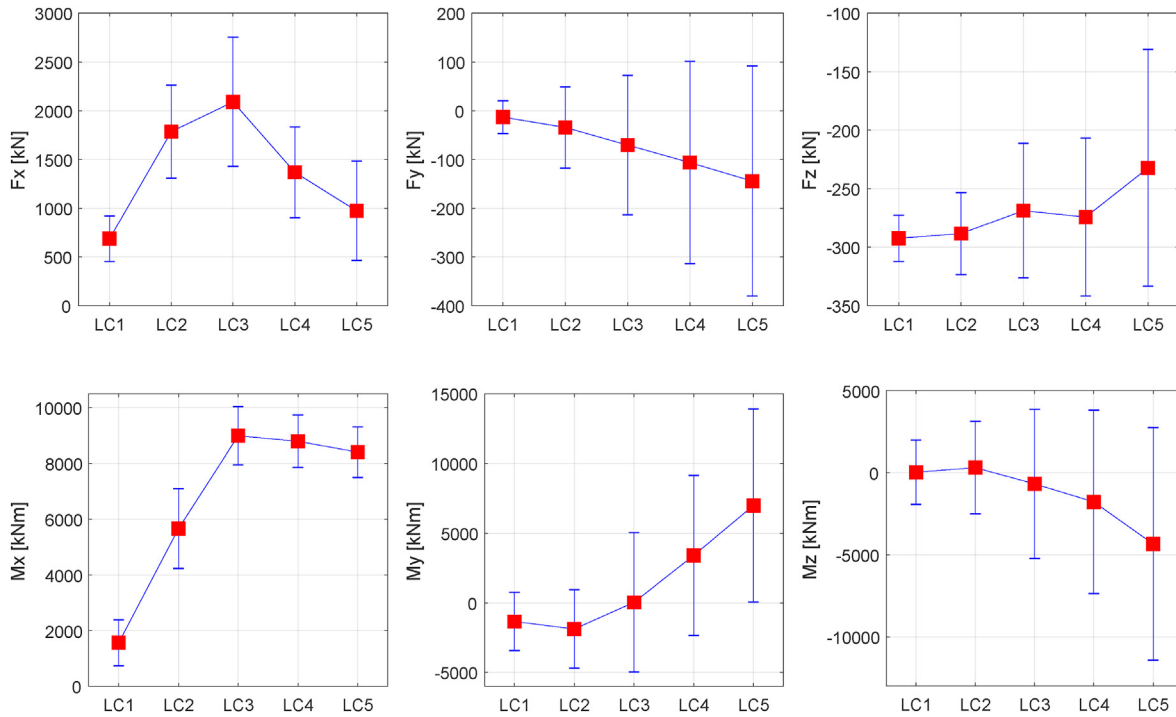


**Fig. 13.** Global response: mean value and standard deviation of forces and moments at hub center under all load cases (The standard deviation is indicated by a range around the mean value.).

in all of the load spectra. In contrast, wave, tower bending resonant as well as the 3P (three blade passing frequency) and the 6P (second harmonic frequency of 3P) induced variations in the forces and moments are relatively small.

### 4.2. Drivetrain load response comparison

In this section, drivetrain gear and bearing load effects for the rigid and the flexible bedplate models are compared. This is expressed by relative load, defined as:

$$\text{relative load} = \frac{L_{\text{Flexible}}}{L_{\text{Rigid}}} \qquad (8)$$

where $L_{\text{Flexible}}$ and $L_{\text{Rigid}}$ are the mean value or standard deviation of gear or bearing loads in flexible and rigid bedplate models, respectively.

Table 8 presents the relative mean values and standard deviations of gear and bearing loads for the rigid and the flexible bedplate models under all load cases. Significant influence of the bedplate flexibility appears in the main bearings, INP-A and INP-B,
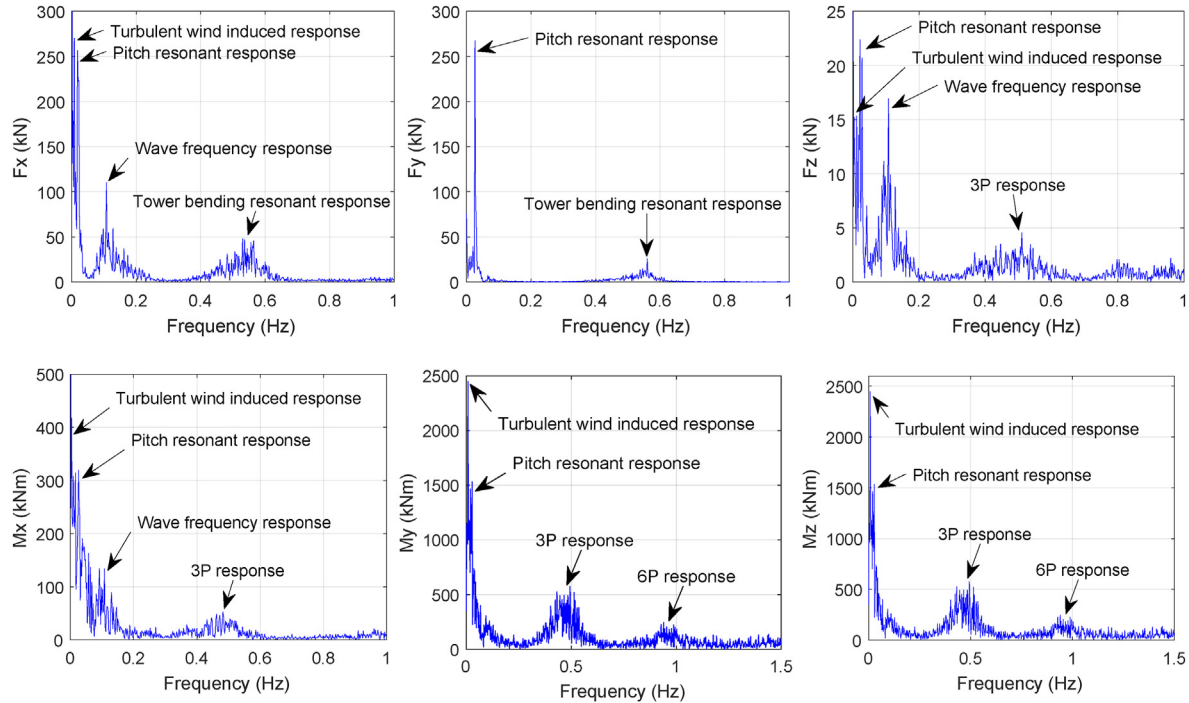
Fig. 14. Global response spectra of forces and moments at hub center under load case LC3.

**Table 8**
Ratio of mean value and standard deviation force response of gears and bearings for flexible bedplate and rigid bedplate.

| Gear, bearing load | Mean value | | | | | Standard deviation | | | | |
|---|---|---|---|---|---|---|---|---|---|---|
| | LC1 | LC2 | LC3 | LC4 | LC5 | LC1 | LC2 | LC3 | LC4 | LC5 |
| INP-A, axial | 0.62 | 0.66 | 0.71 | 0.76 | 0.85 | 0.96 | 0.85 | 0.88 | 1.07 | 1.19 |
| INP-A, radial | 0.61 | 0.59 | 0.72 | 0.82 | 0.88 | 0.83 | 0.74 | 0.74 | 0.83 | 0.89 |
| INP-B, axial | 1.02 | 1.03 | 1.02 | 1.02 | 1.01 | 1.34 | 1.18 | 1.14 | 1.23 | 1.47 |
| INP-B, radial | 1.79 | 1.66 | 1.25 | 1.07 | 0.98 | 0.86 | 0.86 | 0.85 | 0.83 | 0.80 |
| PLC-A, axial | 0.78 | 0.73 | 0.73 | 0.82 | 0.90 | 6.84 | 6.47 | 6.53 | 8.22 | 8.94 |
| PLC-A, radial | 7.36 | 5.37 | 3.37 | 2.29 | 1.61 | 1.56 | 1.30 | 1.04 | 0.79 | 0.75 |
| PLC-B, radial | 3.64 | 3.34 | 2.40 | 1.74 | 1.54 | 2.43 | 2.34 | 2.15 | 1.75 | 1.54 |
| IMS-PLC-A, axial | 1.00 | 1.00 | 1.00 | 1.00 | 1.00 | 1.04 | 1.01 | 1.12 | 1.11 | 1.23 |
| IMS-PLC-A, radial | 3.44 | 3.15 | 1.97 | 1.32 | 1.22 | 2.41 | 2.24 | 1.85 | 1.34 | 1.30 |
| IMS-PLC-B, axial | 1.00 | 1.00 | 1.00 | 1.00 | 1.00 | 1.04 | 0.92 | 1.12 | 1.11 | 1.23 |
| IMS-PLC-B, radial | 1.89 | 1.77 | 1.58 | 1.44 | 1.40 | 1.54 | 1.45 | 1.61 | 1.57 | 1.52 |
| IMS-A, axial | 1.00 | 1.00 | 1.00 | 1.00 | 1.00 | 1.27 | 1.05 | 1.21 | 1.27 | 1.53 |
| IMS-A, radial | 1.05 | 1.03 | 1.06 | 1.00 | 1.05 | 1.08 | 1.15 | 1.31 | 1.35 | 1.35 |
| IMS-B, axial | 1.00 | 1.00 | 1.00 | 1.00 | 1.00 | 1.27 | 1.05 | 1.21 | 1.27 | 1.53 |
| IMS-B, radial | 1.23 | 1.11 | 1.06 | 1.04 | 1.01 | 1.07 | 1.03 | 1.26 | 1.27 | 1.30 |
| HS-A, radial | 1.72 | 2.64 | 3.85 | 3.03 | 2.06 | 1.41 | 1.43 | 1.79 | 1.83 | 1.54 |
| HS-B, axial | 2.74 | 2.17 | 1.77 | 1.54 | 1.31 | 2.33 | 2.20 | 4.15 | 4.41 | 5.48 |
| HS-B, radial | 1.27 | 1.14 | 1.85 | 1.07 | 1.30 | 1.36 | 1.21 | 1.79 | 1.21 | 1.42 |
| $1^{st}$, sun-planet | 1.12 | 1.02 | 1.00 | 1.00 | 1.01 | 1.15 | 1.04 | 1.20 | 1.19 | 1.28 |
| $2^{nd}$, sun-planet | 1.00 | 1.00 | 1.00 | 1.00 | 1.00 | 1.13 | 1.03 | 1.16 | 1.13 | 1.14 |
| $3^{rd}$, gear-pinion | 1.01 | 1.00 | 1.00 | 1.00 | 1.00 | 1.01 | 1.01 | 1.10 | 1.08 | 1.10 |

Green value (< 1.0): decrease; Yellow value (2.0–4.0): slight increase; Pink value (4.0–6.0): moderate increase; Red value (> 6.0): severe increase.

gearbox low-speed stage and high-speed stage bearings, PLC-A, PLC-B, HS-A and HS-B, while much less influence is observed at the gearbox medium-speed bearings, IMS-PLC-A, IMS-PLC-B, IMS-A and IMS-B, and gears of the three stages. The full name of the gears and bearings and their locations in the drivetrain model are presented in Figs. 2 and 3. In general, the flexible bedplate model results in slightly lower main bearing loads compared to the rigid bedplate model, which is induced by the bedplate deformation. Additionally, there is a general increase in the mean value of the bearing radial loads associated with the low-speed and the high-speed stages, namely, PLC-A, PLC-B, HS-A, even in the medium-

speed stage, namely, IMS-PLC-A in the flexible bedplate model. The primary reason is that the deformation of the flexible bedplate causes the misalignment between the main shaft and gearbox low-speed planet carrier as well as between the generator coupling and the gearbox high-speed shaft.

Bedplate flexibility is seen to significantly increase the standard deviation of the axial force of the bearing PLC-A in the flexible bedplate model under all load cases. Additionally, standard deviations of bearing PLC-B radial force and the HS-B axial force are higher in the flexible bedplate model. In contrast, smaller standard deviations are observed in the bearing INP-A axial and radial forces

as well as the INP-B radial force. The reasons for these differences of gear and bearing load variations are revealed by FFT analysis, as shown in Fig. 15. In all of the load spectra, the main response peaks can be categorized into two types: external load response and internal drivetrain resonant response. The external load response includes the low frequency turbulent wind induced response, platform pitch resonant response, wave frequency response as well as the rotor 3P response. This is caused by the external loads that are applied at hub center. The drivetrain resonant response mainly appears at the frequencies 2.98 Hz and 5.13 Hz in the rigid bedplate model and at the frequencies 2.72 Hz and 4.54 Hz in the flexible bedplate model, which corresponds well with the drivetrain eigenfrequencies in coupled rotor-drivetrain-bedplate-tower modes as illustrated in Fig. 9. The drivetrain resonant response is primarily caused by rotor bending moments $M_y$ and $M_z$ at the hub center.

Compared to the rigid bedplate model, the bedplate vertical bending mode is added in the flexible bedplate model, which results in large bedplate deformation and misalignment in gearbox interface positions, and thus larger load effects of gears and bearings inside the gearbox. In the $F_x$ and $F_z$ spectra of the bearing INP-A and $F_y$ spectrum of the bearing INP-B, responses at the turbulent wind frequency, wave frequency as well as the 3P frequency are smaller in the flexible bedplate model than in the rigid model, which means less non-torque loads from the rotor side are carried by main bearings in the flexible bedplate model. Conversely, more non-torque loads would enter into gearbox in the flexible model, which can be observed in the load spectra of bearings PLC-A, PLC-B and HS-A. Another observation is that in the axial force $F_x$ spectra of the bearing PLC-A and HS-B, very small drivetrain resonant response peaks are noticed in the rigid bedplate model compared to the flexible bedplate model. This implies that in the rigid bedplate model, the drivetrain resonance only affects bearing radial load response, while in the flexible model, because of the coupled resonant modes, the drivetrain resonance would also increase bearing axial force response.

### 4.3. Fatigue damage comparison

In this section, 1-h DEFS of gears and DEFL of bearings are compared between the rigid and the flexible bedplate models. This is expressed by relative damage, defined as:

$$\text{relative damage} = \frac{D_{\text{Flexible}}}{D_{\text{Rigid}}} \tag{9}$$

where $D_{\text{Flexible}}$ and $D_{\text{Rigid}}$ are the 1-h DEFS of gears or DEFL of bearings in flexible and rigid bedplate models, respectively.

From equation (5), it is known that for a specific bearing, the fatigue damage is determined by the dynamic equivalent load $P$ and load cycles, where $P$ is determined by axial force and radial force as well as their loading factors. This implies the contributions of axial force and radial force on fatigue damage differ in different bearings. Moreover, at different locations in a drivetrain model, the main reason for the bearing fatigue damage is different. In the low rotational speed locations, the fatigue damage is mainly induced by large loads, while in the high rotational speed locations, it is mainly caused by high number of cycles. Fig. 16 compares bearing load duration distribution and damage equivalent fatigue load (DEFL) of the rigid and the flexible bedplate models under LC3, where bearings INP-A and PLC-A are used as examples to account for the difference of their fatigue damage. For the bearing INP-A, the equivalent load $P$ is calculated from equation (3) as $P = F_r$, thus the radial force determines the equivalent load. From Table 8, both the mean value and standard deviation responses of the radial force are larger in the rigid bedplate model than in the flexible model, which results in the higher fatigue damage of the bearing in the rigid bedplate model. In addition, for the bearing PLC-A, the equivalent
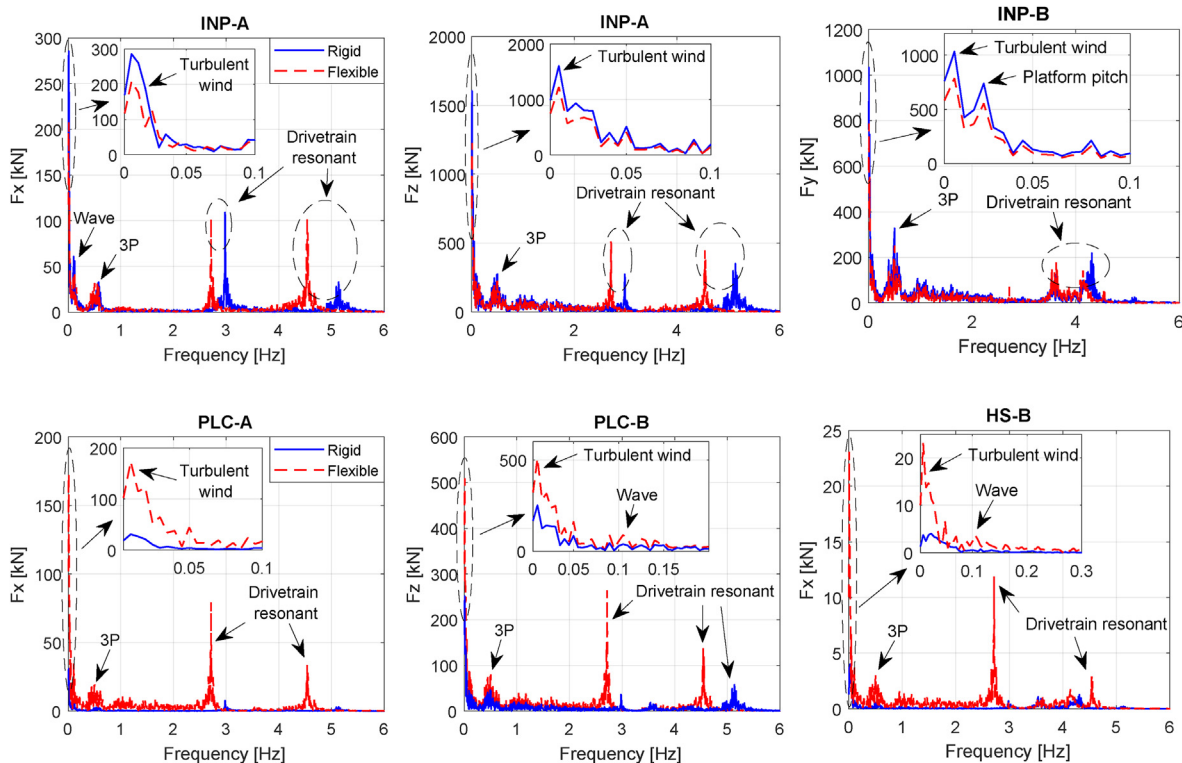


**Fig. 15.** Comparison of bearing load spectra of the rigid and the flexible bedplate models under LC3.
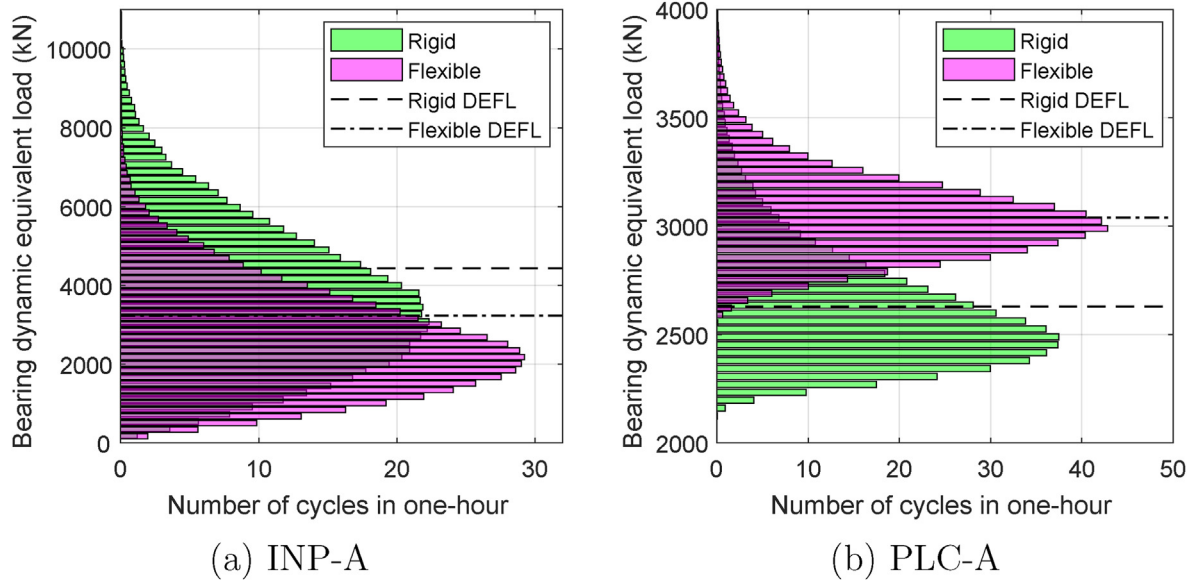
**Fig. 16.** Comparison of bearing load duration distribution and damage equivalent fatigue load (DEFL) of the rigid and the flexible bedplate models under LC3.

load P is expressed as $P = F_r + 1.18F_a$, thus both the axial and radial forces impact significantly the dynamic equivalent load.

Table 9 presents the relative DEFS of gears and DEFL of bearings between the rigid and the flexible bedplate models under all load cases. Significant increases in fatigue damage due to bedplate flexibility are observed at gearbox low-speed stage bearing PLC-B and high-speed stage bearing HS-A. Conversely, there are decreases in fatigue damage of main bearing INP-A. Moreover, small increases are observed in bearings PLC-A, IMS-PLC-B, IMS-A, IMS-B and three-stage gears. The results imply bedplate flexibility would result in a lower fatigue damage in upwind main bearing compared to the rigid bedplate model, and would lead to higher fatigue damage in low-speed stage and high-speed stage bearings in gearbox, while it does not affect the fatigue damage of gears in three-stage and bearings in medium-speed stage of gearbox.

### 4.4. Sensitivity analysis of bedplate modelling fidelity

In this section, the effect of varying fidelity of bedplate modelling on drivetrain fatigue damage is studied with the intent of choosing a reasonable bedplate model for drivetrain dynamic analysis. This study is carried out through six group comparisons, namely, rigid model vs. 5 modes, 5 modes vs. 10 modes, 10 modes vs. 15 modes, 15 modes vs. 20 modes, 20 modes vs. 25 modes and 25 modes vs. 30 modes. The comparison in each group is expressed by percentage difference, $\chi$, of 1-h gear DEFS and bearing DEFL or computational time, defined as:

$$\chi = \frac{D_j - D_i}{D_i} \times 100 \tag{10}$$

where $D_j$ and $D_i$ are the 1-h DEFS of gears or DEFL of bearings or computational time in different mode bedplate models; $j$ represents 30, 25, 20, 15, 10 and 5, while $i$ represents 25, 20, 15, 10, 5 and rigid, respectively. The absolute percentage difference is considered for DEFS of gears and DEFL of bearings.

The results under load case LC3 are presented in Table 10. The largest DEFS or DEFL percentage difference in each group is marked, which shows all of them occur at the high-speed stage bearings HS-A and HS-B. This implies different bedplate models have significant influence on high-speed stage bearing fatigue damage. The largest percentage differences in gear DEFS and bearing DEFL are generally between rigid and 5 mode flexible bedplate models, while much smaller differences are noticed among the other groups. The maximum DEFS or DEFL differences between models with more than 15 modes are lower than 5%, while the computational time is monotonically increasing with the increases of the bedplate modelling fidelity. The findings here imply that it is important to consider the bedplate as a flexible body with high modes when conducting drivetrain dynamic response analysis. It also suggests that if savings in computational costs are desired, modelling bedplate with flexible body that only contains 15 modes could serve as a reasonable load effects evaluation.

### 5. Concluding remarks

This study deals with the effect of bedplate flexibility on drivetrain dynamics through a case study of the DTU 10 MW wind turbine supported on a spar-type structure. The 10 MW drivetrain bedplate is designed in a simplified manner based on extreme design loads and ultimate limit state (ULS) design criteria. A

**Table 9**
Ratio of DEFS of gears and DEFL of bearings for flexible bedplate and rigid bedplate.

| Components | Relative fatigue damage | | | | |
|---|---|---|---|---|---|
| | LC1 | LC2 | LC3 | LC4 | LC5 |
| INP-A | 0.66 | 0.63 | 0.73 | 0.82 | 0.88 |
| INP-B | 1.54 | 1.41 | 1.10 | 0.99 | 0.92 |
| PLC-A | 1.24 | 1.21 | 1.15 | 1.11 | 1.07 |
| PLC-B | 3.32 | 3.03 | 2.30 | 1.75 | 1.54 |
| IMS-PLC-A | 2.10 | 1.76 | 1.38 | 1.16 | 1.15 |
| IMS-PLC-B | 1.16 | 1.09 | 1.06 | 1.04 | 1.04 |
| IMS-A | 1.02 | 0.98 | 1.04 | 1.07 | 1.11 |
| IMS-B | 1.15 | 1.11 | 1.07 | 1.05 | 1.04 |
| HS-A | 1.70 | 2.44 | 3.10 | 2.53 | 1.80 |
| HS-B | 1.34 | 1.22 | 1.14 | 1.16 | 1.35 |
| $1^{st}$, sun | 1.02 | 1.04 | 1.03 | 1.02 | 1.04 |
| $2^{nd}$, sun | 0.98 | 1.02 | 1.04 | 1.02 | 1.02 |
| $3^{rd}$, gear | 0.93 | 0.99 | 1.02 | 1.01 | 1.01 |

Green value (< 1.0): decrease; Yellow value (1.5−3.0): less severe increase; Red value (> 3.0): severe increase.

**Table 10**
Comparisons of bedplate modelling fidelity under LC3 (%difference of DEFS, DEFL or computational time).

| Components | DEFS or DEFL percentage difference | | | | | |
|---|---|---|---|---|---|---|
| | rigid vs. 5 | 5 vs. 10 | 10 vs. 15 | 15 vs. 20 | 20 vs. 25 | 25 vs. 30 |
| INP-A | 5.33 | 4.14 | 0.50 | 0.02 | 0.07 | 0.75 |
| INP-B | 4.86 | 8.83 | 1.41 | 0.26 | 0.08 | 0.10 |
| PLC-A | 20.40 | 0.98 | 2.06 | 0.15 | 0.20 | 0.51 |
| PLC-B | 71.65 | 14.77 | 1.65 | 0.39 | 0.58 | 0.20 |
| IMS-PLC-A | 18.38 | 8.48 | 0.89 | 0.18 | 0.14 | 0.17 |
| IMS-PLC-B | 1.98 | 0.93 | 0.08 | 0.02 | 0.03 | 0.08 |
| IMS-A | 3.84 | 1.99 | 1.16 | 0.19 | 0.96 | 0.53 |
| IMS-B | 2.06 | 0.90 | 0.05 | 0.02 | 0.04 | 0.23 |
| HS-A | 145.84 | 11.82 | 9.60 | 0.14 | 1.13 | 1.31 |
| HS-B | 18.95 | 16.91 | 5.89 | 0.58 | 0.68 | 2.21 |
| $1^{st}$, sun-planet | 0.32 | 0.41 | 0.04 | 0.01 | 0.04 | 0.04 |
| $2^{nd}$, sun-planet | 0.61 | 0.41 | 0.03 | 0.01 | 0.05 | 0.10 |
| $3^{rd}$, gear-pinion | 0.06 | 0.04 | 0.03 | 0.00 | 0.03 | 0.06 |
| Computational time | 18.56 | 2.91 | 2.46 | 3.14 | 4.76 | 4.85 |

Green value ($< 5$): low difference; Yellow value (5–100): medium difference; Red value ($> 100$): high difference.

decoupled approach is employed to study the load effects of a detailed multibody drivetrain model. First, an aero-hydro-servo-elastic simulation of the 10 MW floating wind turbine is carried out to obtain the global response, followed by a local analysis of the drivetrain with forces and moments on the hub center based on the global analysis. Statistical and spectral responses as well as fatigue damage of gears and bearings obtained with the rigid and the flexible bedplate models are compared. Moreover, sensitivity analysis of the bedplate modelling fidelity is conducted. The main conclusions are summarized as follows:

- Compared to the rigid bedplate model, the flexible bedplate model result in bearings inside the gearbox carrying larger loads and fatigue damage, while it reduces the loads and fatigue damage carried by main bearings, and it does not affects gear tooth forces and fatigue damage in the three stages of the gearbox.
- Bedplate flexibility changes the coupled rotor-drivetrain-bedplate-tower eigenmodes, which makes the gearbox resonant response larger compared to that of the rigid bedplate model.
- To achieve acceptable accuracy of fatigue damage in drivetrain gears and bearings, it seems to be necessary to model at least 15 modes of the drivetrain bedplate.

Based on this study, it is recommended to model the bedplate as a flexible structure during the drivetrain dynamic analysis, rather than rigid as in the traditional dynamic analysis approach. Moreover, a multi-dimensional resonant check is recommended to be conducted as resonant response might appear in the non-torsional directions excited by non-torque loads.

### CRediT authorship contribution statement

**Shuaishuai Wang:** Conceptualization, Methodology, Software, Formal analysis, Writing - original draft. **Amir R. Nejad:** Conceptualization, Writing - review & editing. **Erin E. Bachynski:** Software, Writing - review & editing. **Torgeir Moan:** Conceptualization, Writing - review & editing.

### Declaration of competing interest

The authors declare that they have no known competing financial interests or personal relationships that could have appeared to influence the work reported in this paper.

### Acknowledgment

### Appendix. Bedplate material properties and design loads

**Table A1**
Material parameters of bedplate and tower.

| Component | Material | Density (kg/m$^3$) | Young's modulus (GPa) | Poisson's **ratio** | Yield strength (MPa) |
|---|---|---|---|---|---|
| Bedplate | QT400-18 A L | 7100 | 169 | 0.275 | 220 |
| Tower | steel S355 | 7855 | 210 | 0.3 | 355 |

**Table A2**
IEC design load cases.

| DLC | Description |
|---|---|
| 1.1 | Power production with normal turbulence conditions |
| 1.3 | Power production with extreme turbulence conditions |
| 2.1 | Power production with control system fault |
| 5.1 | Emergency shut down with grid loss and with control system fault |
| 6.1 | Parked with extreme wind speed (50-year recurrence) |

**Table A3**
DTU 10 MW reference wind turbine extreme loads.

| DLC | Type | $F_x$ (kN) | $F_y$ (kN) | $F_z$ (kN) | $M_x$ (kNm) | $M_y$ (kNm) | $M_z$ (kNm) |
|---|---|---|---|---|---|---|---|
| DLC1 | Maximum | 7884.80 | −759.81 | −1971.20 | 15303.68 | −3799.04 | 19174.40 |
| DLC2 | Minimum | −4981.76 | 2741.76 | −1680.90 | 6218.24 | −29388.80 | −6200.32 |
| DLC3 | Maximum | −4551.68 | 3852.80 | −191.74 | 5662.72 | −8332.80 | −22400.13 |
| DLC4 | Minimum | −2114.56 | −3709.44 | 474.88 | 7938.56 | 9856.00 | 11612.16 |
| DLC5 | Maximum | −1078.78 | −302.85 | 3584.00 | 7866.88 | −11630.10 | −1953.28 |
| DLC6 | Minimum | −2759.68 | 256.27 | −3727.36 | 3021.12 | −18278.40 | 13905.92 |
| DLC7 | Maximum | 4462.08 | 655.87 | −2347.52 | 19174.40 | 3834.88 | −2240.27 |
| DLC8 | Minimum | 1200.40 | 548.21 | 1.77 | −6984.10 | −9726.50 | −35534.00 |
| DLC9 | Maximum | 873.52 | −456.16 | −578.27 | 12764.00 | 59006.00 | 5753.50 |
| DLC10 | Minimum | 874.50 | 881.66 | 1473.02 | 8061.00 | −52147.20 | 28313.60 |
| DLC11 | Maximum | −2688.00 | −1827.84 | −1768.71 | −9139.20 | 2741.76 | 46950.40 |
| DLC12 | Minimum | 2885.12 | −1784.83 | 817.15 | 11665.92 | −9157.12 | −49638.40 |

The extreme design load cases (DLCs) are selected based on the international standard IEC 61400−3 [45] in this study. The DLCs include conditions of power production, power production with occurrence of fault, emergency shut down with grid loss and with control system fault as well as parked, which are listed in Table A2. Each DLC has been run multiple times with different wind conditions or wave seeds. Table A3 lists the extreme forces and moments from those simulations with consideration safety factors defined in IEC 61400−3 [45], where the coordinate is consistent with that in Fig. 8. In each row, when individual hub center force or moment is the maximum or the minimum value, the other forces and moments are the correspondingly instantaneous values.
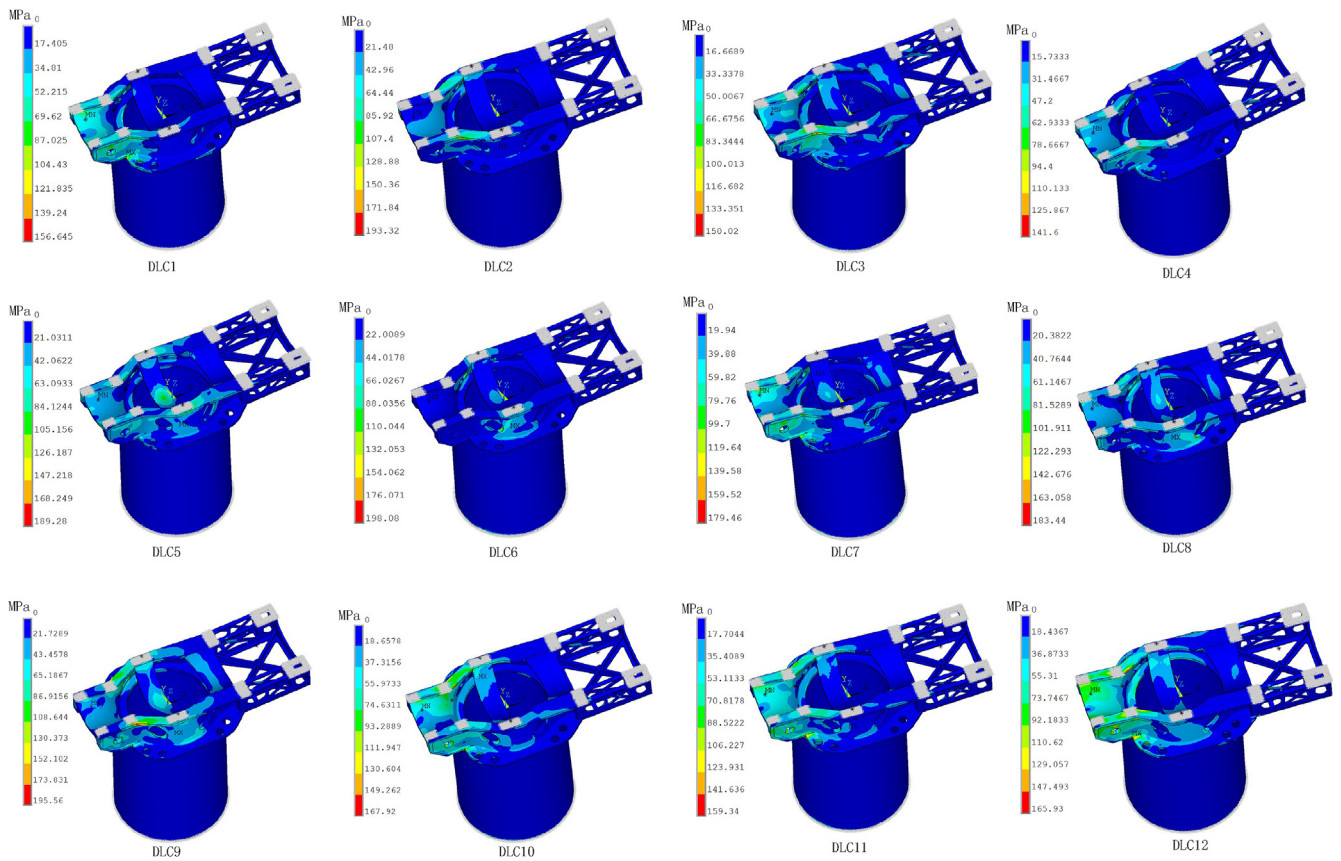


**Fig. 17.** von Mises stress distributions of the bedplate under all design load cases.

# References

[1] Hywind. https://www.equinor.com/en/what-we-do/hywind-where-the-wind-takes-us.html#floating-wind. Online; accessed October 11, 2017.

[2] J.M. Jonkman, Dynamics modeling and loads analysis of an offshore floating wind turbine, in: Tech. rep., National Renewable Energy Lab.(NREL), Golden, CO (United States), 2007.

[3] J. Jonkman, D. Matha, Dynamics of offshore floating wind turbines−−analysis of three concepts, Wind Energy 14 (4) (2011) 557−569.

[4] E.E. Bachynski, L. Eliassen, The effects of coherent structures on the global response of floating offshore wind turbines, Wind Energy 22 (2) (2019) 219−238.

[5] J.M. Hegseth, E.E. Bachynski, A semi-analytical frequency domain model for efficient design evaluation of spar floating wind turbines, Mar. Struct. 64 (2019) 186−210.

[6] J. Carroll, A. McDonald, D. McMillan, Failure rate, repair time and unscheduled O&M cost analysis of offshore wind turbines, Wind Energy 19 (6) (2016) 1107−1119.

[7] Y. Xing, M. Karimirad, T. Moan, Effect of spar-type floating wind turbine

nacelle motion on drivetrain dynamics, Proc. EWEA (2012) (annual event).

[8] Y. Xing, M. Karimirad, T. Moan, Modelling and analysis of floating spar-type wind turbine drivetrain, Wind Energy 17 (4) (2014) 565–587.

[9] A.R. Nejad, E.E. Bachynski, M.I. Kvittem, C. Luan, Z. Gao, T. Moan, Stochastic dynamic load effect and fatigue damage analysis of drivetrains in land-based and TLP, spar and semi-submersible floating wind turbines, Mar. Struct. 42 (2015) 137–153.

[10] A.R. Nejad, E.E. Bachynski, T. Moan, Effect of axial acceleration on drivetrain responses in a spar-type floating wind turbine, J. Offshore Mech. Arctic Eng. 141 (3) (2019), 031901–1.

[11] Z. Li, B. Wen, K. Wei, W. Yang, Z. Peng, W. Zhang, Flexible dynamic modeling and analysis of drive train for Offshore Floating Wind Turbine, Renew. Energy 145 (2020) 1292–1305.

[12] J. Jonkman, S. Butterfield, W. Musial, G. Scott, Definition of a 5-MW reference wind turbine for offshore system development, in: National Renewable Energy Laboratory, Golden, Tech. rep., CO, Technical Report No. NREL/TP-500-38060, 2009.

[13] C. Bak, F. Zahle, R. Bitsche, T. Kim, A. Yde, L. C. Henriksen, A. Natarajan, M. H. Hansen, reportDescription of the DTU 10 MW Reference Wind Turbine, DTU Wind Energy Report-I-0092 5.

[14] J. Jonkman, Definition of the Floating System for Phase IV of OC3 (No. NREL/TP-500-47535), National Renewable Energy Lab (NREL). Golden, CO, USA.

[15] S. Wang, A.R. Nejad, T. Moan, On initial design and modelling of a 10 MW medium speed drivetrain for offshore wind turbines, J. Phys.: Conf. Ser. 1356 (2019), 012024. IOP Publishing.

[16] S. Wang, A.R. Nejad, T. Moan, On design, modelling, and analysis of a 10-MW medium-speed drivetrain for offshore wind turbines, Wind Energy 23 (4) (2020) 1099–1117.

[17] IEC61400-4, Wind Turbines, Part 4: Standard for Design and Specification of Gearboxes, International Electrotechnical Commission: Geneva, Switzerland.

[18] IEC61400-1, Wind Turbines, Part 1: Design Requirements, International Electrotechnical Commission: Geneva, Switzerland.

[19] SIMPACK, Multi-body system software. https://www.3ds.com/products-services/simulia/products/simpack/. Accessed June 16, 2019.

[20] MARINTEK, SIMO User's Manual, MARINTEK, 2011.

[21] MARINTEK, RIFLEX User's Manual, MARINTEK, 2011.

[22] H. Ormberg, E. Passano, N. Luxcey, Global analysis of a floating wind turbine using an aero-hydro-elastic model: Part 1 - code development and case study, in: ASME 2011 30th International Conference on Ocean, Offshore and Arctic Engineering, American Society of Mechanical Engineers, 2011, pp. 837–847.

[23] N. Luxcey, H. Ormberg, E. Passano, Global analysis of a floating wind turbine using an aero-hydro-elastic numerical model: Part 2 - benchmark study, in: ASME 2011 30th International Conference on Ocean, Offshore and Arctic Engineering, American Society of Mechanical Engineers, 2011, pp. 819–827.

[24] A.N. Robertson, F. Wendt, J.M. Jonkman, W. Popko, M. Borg, H. Bredmose, F. Schlutter, J. Qvist, R. Bergua, R. Harries, et al., OC5 Project Phase Ib: validation of hydrodynamic loading on a fixed, flexible cylinder for offshore wind applications, Energy Procedia 94 (2016) 82–101.

[25] F. Oyague, Gearbox modeling and load simulation of a Baseline 750-kW wind turbine using state-of-the-art simulation codes NREL, Tech. rep. (2009). TP-500-41160.

[26] W. LaCava, Y. Xing, Y. Guo, T. Moan, Determining wind turbine gearbox model complexity using measurement validation and cost comparison, in: Tech. rep., National Renewable Energy Lab.(NREL), Golden, CO (United States), 2012.

[27] Z. Jiang, Y. Xing, W. Dong, T. Moan, Z. Gao, Long-term probability distribution of wind turbine planet roller bearing loads, in: WINDPOWER 2013 Conference & Exhibition, 2013, pp. 1–21.

[28] A.R. Nejad, Y. Xing, Y. Guo, J. Keller, Z. Gao, T. Moan, Effects of floating sun gear in a wind turbine's planetary gearbox with geometrical imperfections, Wind Energy 18 (12) (2015) 2105–2120.

[29] Y. Guo, J. Keller, W. LaCava, Planetary gear load sharing of wind turbine drivetrains subjected to non-torque loads, Wind Energy 18 (4) (2015) 757–768.

[30] R. Craig, M. Bampton, Coupling of substructures for dynamic analyses, AIAA J. 6 (7) (1968) 1313–1319.

[31] J. Helsen, F. Vanhollebeke, B. Marrant, D. Vandepitte, W. Desmet, Multibody modelling of varying complexity for modal behaviour analysis of wind turbine gearboxes, Renew. Energy 36 (11) (2011) 3098–3113.

[32] J. Helsen, B. Marrant, F. Vanhollebeke, F. De Coninck, D. Berckmans, D. Vandepitte, W. Desmet, Assessment of excitation mechanisms and structural flexibility influence in excitation propagation in multi-megawatt wind turbine gearboxes: experiments and flexible multibody model optimization, Mech. Syst. Signal Process. 40 (1) (2013) 114–135.

[33] X. Jin, L. Li, W. Ju, Z. Zhang, X. Yang, Multibody modeling of varying complexity for dynamic analysis of large-scale wind turbines, Renew. Energy 90 (2016) 336–351.

[34] W. Dong, C. Zhu, C. Song, H. Han, Effects of elastic support on the dynamic behaviors of the wind turbine drive train, Front. Mech. Eng. 12 (3) (2017) 348–356.

[35] W. Dong, Y. Xing, T. Moan, Z. Gao, Time domain-based gear contact fatigue analysis of a wind turbine drivetrain under dynamic conditions, Int. J. Fatig. 48 (2013) 133–146.

[36] A.R. Nejad, Z. Gao, T. Moan, Long-term analysis of gear loads in fixed offshore wind turbines considering ultimate operational loadings, Energy Procedia 35 (2013) 187–197.

[37] Z. Jiang, Y. Xing, Y. Guo, T. Moan, Z. Gao, Long-term contact fatigue analysis of a planetary bearing in a land-based wind turbine drivetrain, Wind Energy 18 (4) (2015) 591–611.

[38] ISO281, Rolling Bearings-Dynamic Load Ratings and Rating Life, International Organization for Standardization: Geneva, Switzerland.

[39] J.E. Shigley, Shigley's Mechanical Engineering Design, Tata McGraw-Hill Education, 2011.

[40] ISO6336-2, Calculation of Load Capacity of Spur and Helical Gears, Part 2: Calculation of Surface Durability (Pitting), International Organization for Standardization: Geneva, Switzerland.

[41] ISO6336-3, Calculation of Load Capacity of Spur and Helical Gears, Part 3: Calculation of Tooth Bending Strength, International Organization for Standardization: Geneva, Switzerland.

[42] ISO6336-5, Calculation of Load Capacity of Spur and Helical Gears, Part 5: Strength and Quality of Materials, International Organization for Standardization: Geneva, Switzerland.

[43] L. Li, Z. Gao, T. Moan, Joint distribution of environmental condition at five european offshore sites for design of combined wind and wave energy devices, J. Offshore Mech. Arctic Eng. 137 (3) (2015), 031901.

[44] B.J. Jonkman, TurbSim User's Guide: Version 1.50, Tech. Rep, National Renewable Energy Lab.(NREL), Golden, CO (United States), 2009.

[45] IEC61400-3, Wind Turbines, Part 3: Design Requirements for Offshore Wind Turbines, International Electrotechnical Commission: Geneva, Switzerland.